# Runaway Electron Transport in Stochastic Toroidal Magnetic Fields

L. Carbajal,[1, a)] D. del-Castillo-Negrete,[2] and J. J. Martinell[1]
[1)] *Instituto de Ciencias Nucleares, UNAM, Mexico City 04510, Mexico*
[2)] *Oak Ridge National Laboratory, Oak Ridge, TN 37831-6304 USA*

(Dated: 17 February 2020)

In this work we study the transport and confinement properties of runaway electrons (RE) in presence of magnetic fields with perturbations producing different levels of stochasticity. We use KORC [L. Carbajal et al., Phys. Plasmas **24**, 042512 (2017); D. del-Castillo-Negrete et al., Phys. Plasmas **25**, 056104 (2018)] for simulating the full-orbit (FO) and guiding-center (GC) dynamics of RE in perturbed magnetic fields that exhibit magnetic islands. We extend previous works on this problem [A. Wingen et al., Nucl. Fusion **46**, 941 (2006); V. A. Izzo et al., Nucl. Fusion **51**, 063032 (2011); G. Papp et al., Nucl. Fusion **51**, 043004 (2011); V. Izzo and P. Parks, Phys. Plasmas **24**, 060705 (2017); C. Sommariva et al., Nucl. Fusion **58**, 016043 (2018)] by studying in detail full-orbit effects on the RE dynamics. We quantify FO effects on RE transport by performing one-to-one comparisons between FO and GC simulations. It is found that, for the magnetic field configurations considered, GC simulations predict twice the RE losses of FO simulations for 1 MeV, and four times the RE losses of FO simulations for 25 MeV. Similarly, we show how different GC and FO dynamics of RE moving around magnetic islands can be, especially in the scenario where the RE Larmor radius is of the order of the size of the magnetic island. We also study the role of rotation of the magnetic islands on RE confinement, we find that low-frequency toroidal rotation has no observable effect on RE transport in the cases considered. These results shed some light into the potential of avoidance or mitigation mechanisms based on magnetic perturbations.

PACS numbers: 52.20.Dq, 52.25.Fi, 52.55.-s, 52.65.-y, 28.52.-s, 89.30.Jj, 52.55.Fa, 02.50.Ey

## I. INTRODUCTION

The avoidance and mitigation of relativistic runaway electrons (RE) with energies of several MeV in magnetic confined fusion plasmas is necessary for the safe operation of future fusion reactors such as ITER[1]. During the past years, important advances in the RE mitigation strategies have been made using massive gas injection[2,3] and shattered pellet injection[4,5] of impurities to mitigate RE using collisional processes. More recently, the use of kinetic instabilities to deconfine RE during the RE plateau[6–9] has been proposed. These advances have been made possible due to the joint efforts of experimental, theoretical and numerical studies.

In this work, we perform a numerical study of the confinement of RE in perturbed toroidal magnetic fields with various levels of stochasticity driven by overlapping of magnetic islands. For low-energy particles, it is known that transport in stochastic fields can be multi-scale[10], spanning fast timescales where drifts dominate to slow timescales where particles diffuse following magnetic field lines. Although RE transport in stochastic magnetic fields might also exhibit multi-scale phenomena, we restrict our study to timescales of up to $\sim 1$ ms, where collisional and synchrotron radiation losses effects do not significantly modify the RE dynamics. The study of RE dynamics during the thermal and current quench is out of the scope of the present work, since this would require the inclusion of collisional, radiation losses, and self-consistent electric field effects as well as the complex dynamics of the magnetic fields (see Fig. 3 of Ref. 11 or Fig. 6 of Ref. 12). Numerical results reported in Ref. 11 are used to construct an analytical model of a perturbed magnetic field that includes MHD-like modes in the equilibrium magnetic field of Refs. 13 and 14. We use KORC[13–15] for following the full-orbit (FO) and guiding-center (GC) dynamics of RE in these perturbed magnetic fields.

Previous numerical studies have analyzed the role of perturbed toroidal magnetic fields on the GC dynamics and confinement of RE[11,14,16–18]. In agreement with experiments, these studies concluded that relatively low-energy RE tend to be less confined than high-energy RE, this due to drift orbit effects in toroidal geometry, which was predicted in early theoretical studies[19]. Other studies of RE transport in perturbed magnetic fields include Ref. 20, where the authors investigated finite Larmor radius (FLR) effects on RE dynamics evolving in micro-turbulence through gyro-kinetic simulations in non-toroidal geometries. In this work the authors also find a reduction in RE transport as the RE energy increases; however, the effect of toroidal geometry is not included. In Ref. 21, the authors studied radial transport driven by magnetic field stochasticity using an orbit-averaged model for the RE dynamics in toroidal geometries. This was done by coupling an advection-diffusion model for the radial transport of RE to the orbit-averaged model. In this advection-diffusion model, the transport coefficients were estimated through Monte-Carlo simulations. More recently, the first FO simulations of RE in perturbed, time-dependent MHD toroidal magnetic fields[12] studied the formation and confinement of RE. In

[a)] leopoldo.carbajal@correo.nucleares.unam.mx

this study it was found that drift orbit effects and parallel transport along open magnetic field lines are responsible for most of the observations on the RE confinement, but a detailed analysis of FO effects for various populations of RE with different energies and pitch angles and different magnetic perturbation amplitudes was not done.

In the present work, we extend previous studies on RE confinement[11,12,16–18] by studying FO effects on RE transport in perturbed toroidal magnetic fields with different levels of stochasticity. We perform one-to-one comparisons of FO and GC simulations to quantitatively assess when both models for the RE dynamics predict similar RE transport, and when FO effects need to be taken into account. We find that FO effects, in particular FLR effects, enhances the confinement of RE in stochastic toroidal magnetic fields with respect to GC simulations, reducing RE losses by a factor of two for 1 MeV RE nd by one-third for 25 MeV. Our results are in agreement with the trends observed in experiments and answer a long-standing question on the full-orbit effects on RE confinement.

The rest of the paper is organized as follows: in Sec. II presents the analytical model for the perturbed magnetic field that is used in our KORC simulations of RE. Also, we present the case studies of the perturbed magnetic field used through this work. In Sec. III we present the plasma parameters considered in this study. In Sec. IV we present the estimate of the variation in our calculations of the number of confined RE due to the finite number of particles in the simulation. Then, in Sec. V we study the RE dynamics in the presence of a single magnetic islands when $r_L$ is varied. A one-to-one comparison between FO and GC simulations is done. It is in Sec. VI that we include both, the full-orbit effects and stochasticity on the RE confinement. A detailed comparison between FO and GC simulations is made here to identify scenarios where FO need to be included. Finally, in Sec. VII we study of RE transport when FO effects, magnetic field stochasticity and the effect of toroidal rotation are included at the same time. We study the dynamics of RE around magnetic islands, and investigate the joint effect of rotation and stochasticity on low- and high- energy RE confinement. In Sec. VIII we present a discussion on our results.

## II. MAGNETIC FIELD MODEL

The model of the magnetic field used in all the simulations reported in this manuscript is a generalization of the analytical field of Refs. 13 and 15, corresponding to a magnetic field of nested circular, toroidal magnetic flux surfaces, which in toroidal coordinates is given by:

$$\boldsymbol{B}(r,\theta) = B_\zeta(r,\theta)\hat{\boldsymbol{e}}_\zeta + B_\theta(r,\theta)\hat{\boldsymbol{e}}_\theta. \tag{1}$$

where $B_\zeta(r,\theta) = Bo/(1+\eta\cos\theta)$ is the toroidal magnetic field, $\eta = r/R_0$ is the inverse aspect ratio, $R_0$ is the major radius at the magnetic axis, $B_0$ is the toroidal magnetic field at $R_0$, and $B_\theta(r) = \kappa\eta B_0/[q(r)(1+\eta\cos\theta)]$ is the poloidal magnetic field. Here $\kappa = \hat{\boldsymbol{J}}_p \cdot \hat{\boldsymbol{e}}_\zeta$ with $\hat{\boldsymbol{J}}_p$ the unit vector in the direction of the toroidal plasma current density. $q(r)$ is the safety factor, given by:

$$q(r) = q_0\left(1+\frac{r^2}{\varepsilon^2}\right). \tag{2}$$

The constant $\varepsilon$ is obtained from the values of $q_0$ and $q(r)$ at the plasma edge $r = a$. The coordinates $(r,\theta,\zeta)$ are defined as $x = (R_0 + r\cos\theta)\sin\zeta$, $y = (R_0 + r\cos\theta)\cos\zeta$, and $z = r\sin\theta$, where $(x,y,z)$ are the Cartesian coordinates. In these coordinates, $r$ denotes the minor radius, $\theta$ the poloidal angle, and $\zeta$ the toroidal angle. Note that in this right-handed toroidal coordinate system, the toroidal angle $\zeta$ rotates clockwise, that is, it is anti-parallel to the azimuthal angle, $\phi = \pi/2 - \zeta$, of the standard cylindrical coordinate system.

The magnetic field of Eq. (1) is perturbed by including MHD-like modes[22,23]. The perturbation to the magnetic field is written in the following form:

$$\delta\boldsymbol{B} = \sum_{mn}\delta\boldsymbol{B}_{mn} = \sum_{mn}\nabla\times\boldsymbol{A}_{mn}\ , \tag{3}$$

where $\boldsymbol{A}_{mn} = \tilde{\alpha}_{mn}(r,\theta,\zeta)R_0\boldsymbol{B}(r,\theta)$, $\boldsymbol{B}(r,\theta)$ is the equilibrium magnetic field of Eq. (1), and the subscripts $m$ and $n$ refer to the poloidal and toroidal numbers of a given mode, respectively. The form of $\delta\boldsymbol{B}$ ensures that the resulting magnetic field is divergence free, and the inclusion of $\boldsymbol{B}(r,\theta)$ in $\boldsymbol{A}_{mn}$ allows us to include perturbations along and across the local magnetic field[22]. The function $\tilde{\alpha}_{mn}(r,\theta,\zeta)$ is given by:

$$\begin{aligned}
\tilde{\alpha}_{mn}(r,\theta,\zeta) &= \alpha_{mn}(r)\cos\varphi_{mn}\ ,\\
\alpha_{mn}(r) &= \epsilon_{mn}f(r)g(r)h(r)\ ,\\
f(r) &= \frac{1}{2}\left[1-\tanh\left(\frac{r-a}{l_{mn}}\right)\right]\ ,\\
g(r) &= \left(\frac{r}{r^*_{mn}}\right)^m\ ,\\
h(r) &= \exp\left[-\frac{(r-r_{mn})^2}{2\sigma^2_{mn}}+\frac{(r^*_{mn}-r_{mn})^2}{2\sigma^2_{mn}}\right]\ ,
\end{aligned} \tag{4}$$

where $\epsilon_{mn}$ is a constant, $\varphi_{mn} = \kappa m\theta - n\zeta + \omega^*_{mn} - \omega_{mn}t$ is the phase of the $(m,n)$ mode, $\omega_{mn}$ is the toroidal rotation frequency of the mode, $t$ is the time, $\omega^*_{mn}$ is an arbitrary initial phase of the mode, $r^*_{mn} = \varepsilon\sqrt{m/nq_0 - 1}$ is the radial position of the mode, $r_{mn} = r^*_{mn} - m\sigma^2_{mn}/r^*_{mn}$, $\sigma_{mn}$ is the width of the mode amplitude, and $l_{mn}$ is the decay rate at the edge of the amplitude of the mode.

Following[22] and references therein, we can calculate the half-width of the magnetic island that produces a $(m,n)$ mode as follows:

$$\delta r_{mn} \approx \sqrt{\frac{4q(r^*_{mn})b(r^*_{mn})R_0}{nq'(r^*_{mn})}} \ , \tag{5}$$

where $q(r^*_{mn})$ and $q'(r^*_{mn})$ are the safety factor and its derivative at the resonance position $r^*_{mn}$, respectively, and $b(r) = \epsilon_{mn}\kappa m R_0 \alpha_{mn}(r^*_{mn})/r^*_{mn}$.

In the cases where toroidal rotation of the perturbation modes is included ($\omega_{mn} \neq 0$), the following inductive electric field is expected to occur:

$$\boldsymbol{E} = -\sum_{m,n} \frac{\partial \boldsymbol{A}_{mn}}{\partial t} \ . \tag{6}$$

As it will be shown below, although this inductive electric field can be relatively large in some cases, its net effect on the RE energy is not significant with respect to the cases where no rotation is included. Also, mode rotation modifies the orbits mostly along the $\theta$ direction, but not radially.

Now, we describe the cases of perturbed magnetic fields that will be used through the the manuscript. In all cases, we use the parameters of the equilibrium magnetic field of Eq. (1) with the parameters of Sec. III, and no rotation is included unless otherwise specified.

- Case 0: We include only one mode, $m = 2$. Its amplitude is set to $\epsilon_{21} = 6.5\times10^{-6}$. This generates a magnetic island with half-width of $\delta r_{21} \approx 0.01$ m, see Eq. (5), and maximum amplitudes $|\delta B_{21}/B_0| \approx 1\times10^{-4}$. The decay rate $l_{21}$ is set to 0.005 m. $\sigma_{21}$ is set to 0.02 m.

- Case 1: The amplitudes $\epsilon_{mn}$ of Eq. (4) are $\epsilon_{21} = 6.5\times10^{-6}$, $\epsilon_{31} = 5.5\times10^{-6}$, $\epsilon_{41} = 5.0\times10^{-6}$, $\epsilon_{51} = 4.5\times10^{-6}$, and $\epsilon_{61} = 4.0\times10^{-6}$. These amplitudes generate magnetic islands with half-width of $\delta r_{mn} \approx 0.01$ m for all modes, see Eq. (5), and with maximum amplitudes of the magnetic field perturbations of $|\delta B_{mn}/B_0| \approx 1\times10^{-4}$. The decay rate $l_{mn}$ is set to 0.005 m for all modes, this gives a fast and smooth drop of any $\delta\boldsymbol{B}_{mn}$ at the plasma edge $r = a$. $\sigma_{mn}$ is set to 0.02 m for all modes. In Fig. 1(a) and (b) we show $\alpha_{mn}$ and Poincaré sections of 1 eV electrons, which approximately follow magnetic field lines.

- Case 2: The amplitudes $\epsilon_{mn}$ are ten times larger than those of Case 1, these amplitudes generate magnetic islands with half-width $\delta r_{mn} \approx 0.034$ m for all modes. The maximum amplitude of $|\delta B_{mn}/B_0| \approx 1\times10^{-3}$. The rest of the mode parameters are the same of Case 1. In Fig. 1(e) we can see significant overlap of $\alpha_{mn}$, which generate broad regions of stochastic regions in particle orbits, see Fig. 1(d). Only for $r < 0.15$ m we observe robust, formed magnetic surfaces.

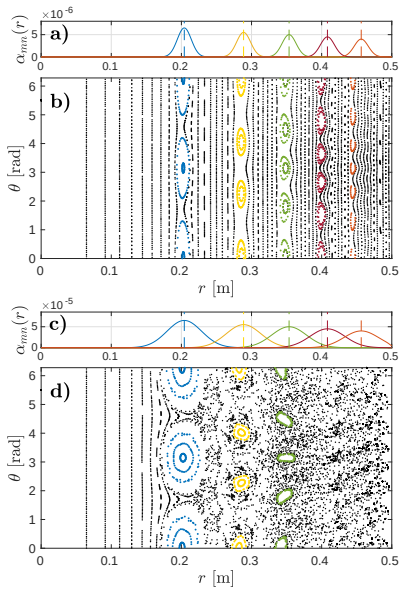


FIG. 1. Mode amplitude and Poincaré sections of low-energy electrons. Panel a): radial amplitude $\alpha_{mn}$ for the modes of Case 1. The vertical dashed lines show $r^*_{mn}$ of Eq. (4). Panel b): Poincaré sections of 1 eV electron orbits streaming along the perturbed magnetic field of Case 1. These low energy electrons approximately follow magnetic field lines. The resulting magnetic islands are highlighted with the same color of their corresponding $\alpha_{mn}$ in panel (a). Panel c): same as panel (a) for Case 2. Panel d): same as panel (b) for Case 2.

A useful parameter to be used to estimate the stochasticity in the magnetic field is the Chirikov parameter[24]:

$$S_{m_1m_2} = \frac{\delta r_{m_1n} + \delta r_{m_2n}}{|r^*_{m_1n} - r^*_{m_2n}|} \ , \tag{7}$$

where $\delta r_{m_1n}$ and $\delta r_{m_2n}$ are the half-width of Eq. (5) for modes with $m = m_1$ and $m = m_2$, respectively. $r^*_{m_1n}$ and $r^*_{m_2n}$ are the corresponding radial positions of the modes. In Fig. 2 we show $S_{m_1m_2}$ for the cases described above. In this figure, the vertical magenta lines show the radial position of the modes $r^*_{mn}$. According to this criterion, if for two adjacent islands $S > 1$, then there are no integrable orbits between the islands. That is, all the orbits in that region are chaotic. It is known that this parameter underestimates the level of stochasticity in the magnetic field, but still provides a good relative measure of stochasticity between the cases studied in this work. From the Poincaré sections of low-energy electrons

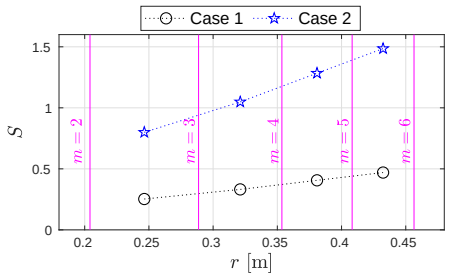


FIG. 2. Chirikov parameter for stochasticity in regions between magnetic islands. The vertical magenta lines show the radial position of the modes $m = 2$ to $m = 6$.

of Fig. 1(d), we observe stochastic regions between the modes of Case 2 for which $S \geq 0.8$.

The Chirikov parameter of Eq. (7) proves to be useful to estimate the stochasticity of the magnetic field and particle orbits when these do no depart greatly from the magnetic field lines, that is, when the particles have low energies and small pitch angles. However, when energetic particles are considered, their orbits depart from the magnetic field lines. In this scenario an heuristic extension of $S_{m_1 m_2}$ for particle orbits might be proposed:

$$\hat{S}_{m_1 m_2} = \frac{\delta r_{m_1 n} + \delta r_{m_2 n} + 2 r_L}{|r^*_{m_1 n} - r^*_{m_2 n}|} \,. \tag{8}$$

Here, $r_L$ is the characteristic Larmor radius of the particle under study. This extension of the Chirikov parameter accounts for both overlapping of magnetic islands (as observed by the particle orbits) and the interaction of the particle orbit (through $r_L$) with two adjacent islands. As for $S_{m_1 m_2}$, $\hat{S}_{m_1 m_2} > 1$ would mean that stochastic orbits of energetic particles (which now depart from magnetic field lines) are expected between resonances $m_1$ and $m_2$. An increase in energy and pitch-angle of the RE will produce larger $r_L$ values, which in turn make $\hat{S}_{m_1 m_2}$ larger than $S_{m_1 m_2}$, that is, $\hat{S}_{m_1 m_2}$ would predict even more stochasticity of RE orbits for high-energy, large pitch-angle RE. As it will be shown in Sec. VI, this is not the case. In fact, FO effects are found to suppress RE losses (with respect to GC orbits following approximately magnetic field lines). One could try to improve the estimate of Eq. (8) by including the shift of the position of the modes $r^*_{mn}$ by taking into account the RE orbits shifts (see Sec. III.A.1 of Ref. 14), but these latter are approximately the same for all RE around two adjacent perturbations; therefore, this effect would be cancelled in the difference $r^*_{m_1 n} - r^*_{m_2 n}$.

## III. PLASMA PARAMETERS

The plasma parameters used in this work correspond to those of a typical medium-size tokamak (e.g. DIII-D), that is, toroidal magnetic field $B_0 = 2$ T, major radius $R_0 = 1.5$ m, plasma radius $a = 0.5$ m, $q_0 = 1$, $q_a = 7$, which corresponds to a plasma current $I_p \sim 250$ kA[11]. The direction of the toroidal magnetic field $\boldsymbol{B}_\zeta$ is along the toroidal direction $\hat{\boldsymbol{e}}_\zeta$, while the plasma current density $\boldsymbol{J}_p$ is anti-parallel to $\hat{\boldsymbol{e}}_\zeta$, therefore $\kappa = -1$ in $B_\theta(r, \theta)$ of Eq. (1). This configuration causes a drift of the RE towards the low-field side (LFS).

The parameters of the magnetic perturbations $\delta \boldsymbol{B}_{mn}$ are chosen so that the widths of the magnetic islands that they produce are the same for all the $(m, n)$ modes. This choice allows us to control island overlapping, and thus the level of stochasticity of the magnetic field, in a simple way. In all the simulations reported in this manuscript, unless stated otherwise, we include modes with $n = 1$ and $m = 2, 3, 4, 5$, and 6. These modes are the ones observed to dominate in MHD simulations of rapid shutdown of DIII-D limited plasmas[11], and are included in our analytical model of the perturbed magnetic field. The amplitude of each mode is specified in Sec. II, and are chosen so that various degrees of island overlapping are obtained. For simplicity, $\omega^*_{mn}$ is set to zero for all the modes in the simulations, arbitrary random values can be used but we do not expect to observe a significant effect on the RE transport. When plasma rotation is included ($\omega_{mn} \neq 0$), we set the toroidal rotation to $f = 50$ kHz, which is equivalent to an angular frequency of $\omega_{mn} = 300$ kHz. This rotation frequency is inferred from the rotation of blobs of synchrotron radiation emitted by RE measured in the TEXTOR tokamak[25], which is a typical medium-size tokamak for which information about toroidal rotation frequency could be found in the literature. As it was shown in Ref. 14, these blobs of synchrotron radiation are due to RE trapped in magnetic islands. We note that this value of $\omega_{mn}$ is not representative of all the scenarios where RE occur in rotation perturbed magnetic fields, but it is a value that can be found in the literature for a medium-size tokamak where RE with several MeV were observed[25].

Regarding the parameters of the simulated RE, their initial energy distributions correspond to mono-energetic and mono-pitch-angle distribution functions $f(\mathcal{E}, \theta) = \delta(\mathcal{E} - \mathcal{E}_0)\delta(\vartheta - \vartheta_0)/\sin\theta$, with $\mathcal{E}_0$ ranging from 1 MeV to 25 MeV, as specified in each case. The values of $\vartheta_0$ are specified in each case. The factor $1/\sin\theta$ in $f(\mathcal{E}, \theta)$ is for normalization purposes. Here, $\cos\vartheta = p_\parallel/p$ with $p$ and $p_\parallel$ the momentum of the simulated RE and its parallel component along the local magnetic field, respectively.

In all the simulations reported in this manuscript, we do not include collisions or synchrotron radiation losses. This is because in the time scales considered ($t \lesssim 1$ ms) these effects have little effect on the RE dynamics[14].

## IV. STATISTICAL CONVERGENCE OF KORC SIMULATIONS

Our KORC simulations, which follow RE orbits in different magnetic fields, are Monte Carlo (MC) simulations that provide estimates of various quantities, e.g. the number of confined RE, $N$, after some time $t$ given an initial condition and magnetic field at $t = 0$. One of the issues when using MC simulations is the amount of "noise" introduced in the calculation of bulk quantities of the plasma due to the finite number of particles used in the simulation[26]. This issue is of particular concern when small variations in bulk plasma quantities are observed and we want to know whether these are due to some physical effect, or simply due to "noise" in our simulation. In all our simulations We take this into account as explained below.

In Fig. 3 we show the number of confined, full-orbit 25 MeV RE in the magnetic field of Eq. (1) after 0.1 ms (filled markers). We set the number of simulation particles $N_{sim}$ to 1,000, 10,000, 100,000, and 500,000 in the simulations reported in this figure. The initial condition for these simulations is the same, the 25 MeV RE are uniformly distributed in a torus of radius 0.3 m centered at the magnetic axis $R_0$. The initial mono-pitch angle distribution of the RE is that all RE have a finite $\vartheta_0 = 40°$, in such order to allow RE to cross magnetic field surfaces, which determines the RE confinement to some degree. We include a set of modes $\delta\boldsymbol{B}_{mn}$ in the magnetic field that corresponds to Case 1 of Sec. II. As it can be seen, the number of confined RE, which has been normalized to $N_{sim}$, shows some fluctuations around $N/N_{sim} = 66\%$ for different simulations with different $N_{sim}$. This is expected, since $N$ is a MC estimate that depends on $N_{sim}$. Following Ref. 26, we can calculate the standard error $\epsilon_N$ in the computation of $N$ due to the finite number of particles in the MC simulation as follows:

$$\epsilon_N = \frac{\sigma_N}{\sqrt{N_{sim}}}\ ,$$
$$\sigma_N^2 = \int\int \left(n(\boldsymbol{v},\boldsymbol{x}) - \langle n(\boldsymbol{v},\boldsymbol{x})\rangle\right)^2 p(\boldsymbol{v},\boldsymbol{x}) d^3\boldsymbol{x} d^3\boldsymbol{v}\ . \tag{9}$$

Here, $\sigma_N$ is the variance of the MC estimate of $N$, $n(\boldsymbol{v},\boldsymbol{x})$ is the number of particles with initial position $\boldsymbol{x}$ and velocity $\boldsymbol{v}$, $p(\boldsymbol{v},\boldsymbol{x})$ is the probability density function that a RE with initial position $\boldsymbol{x}$ and velocity $\boldsymbol{v}$ remains confined by the end of the simulation. The average $\langle\cdot\rangle$ represents the ensemble average over all particles in the simulation. The integral of Eq. (9) is calculated numerically, the toroidal geometry of the problem is taken into account by using toroidal coordinates. Here, $p(\boldsymbol{v},\boldsymbol{x})$ is calculated numerically by binning the initial position in phase space of those RE that by the end of the simulation remain confined. In Fig. 3 we show the estimate of $N$ with filled markers and $N \pm \epsilon_N$ with error bars. As expected, the confidence interval $N \pm \epsilon_N$ for a given value of $N_{sim}$ is within or it overlaps the confidence interval for smaller $N_{sim}$. This shows how the MC estimate $N$ converges as $N_{sim}$ increases, and allows us to identify when a variation of a bulk plasma quantity is due to MC "noise" or due to some physical process.

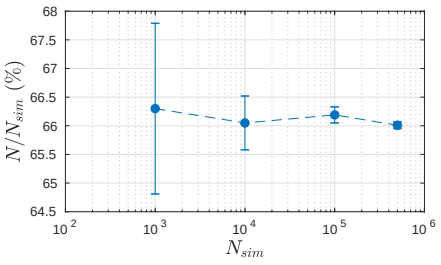


FIG. 3. Monte Carlo estimate of the number of confined 25 MeV RE in a perturbed magnetic field, $N$. The MC estimate of $N$ is shown with filled markers for different values of $N_{sim}$. The confidence interval $N \pm \epsilon_N$ is shown with error bars. We set $N_{sim}$ to 1,000, 10,000, 100,000, and 500,000 in these four simulations. The structure of $\delta\boldsymbol{B}_{mn}$ corresponds to Case 1 of Sec. II.

## V. RE TRANSPORT IN THE PRESENCE OF MAGNETIC ISLANDS

In this section we study the dynamics of RE around a magnetic island when its energy and pitch-angle are varied, and therefore its Larmor radius is changed. For this, it is useful to use the characteristic RE Larmor radius $r_L = v_\perp/\Omega_e$ to compare the length scales of the gyromotion of the RE with the length scales of the magnetic field, that is, the half-width of the magnetic islands of Eq. (5). Here, $v_\perp$ and $\Omega_e = eB_0/\gamma m_e$ are the perpendicular velocity and relativistic cyclotron frequency of RE. In Fig. 4 we show the RE Larmor radius for various values of their pitch angle $\vartheta$ as function of their kinetic energy $\mathcal{E}_0$ (dashed lines). The solid horizontal lines in this figure show the values of the half-width of the magnetic islands produced in each case described in Sec. II. This figure thus allows us to see the relationship between $r_L$ and $\delta r_{mn}$ for various magnetic field and RE parameters.

We investigate the full-orbit effects on the RE dynamics in perturbed fields by performing a one-to-one comparison between FO and GC simulations of 10 MeV RE in the perturbed magnetic field of Case 0 varying their initial pitch-angle, which is equivalent to vary their characteristic Larmor radius and magnetic moment, see Appendix. A. In Fig. 5(a) we show a close-up of the islands of the $(m,n) = (2,1)$ mode in the Poincaré sections of 1 eV electrons in the magnetic field of Case 0. These low-energy electrons approximately follow magnetic field

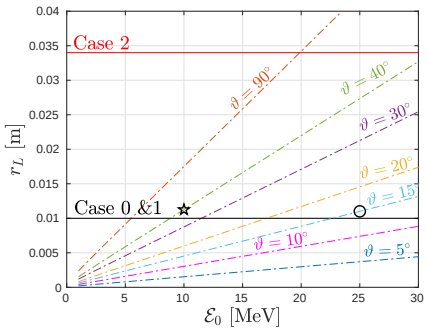


FIG. 4. Runaway electron Larmor radius $r_L$ for various pitch angles $\vartheta$ as function of their energy $\mathcal{E}_0$. The horizontal solid lines show the half-width of the islands of the perturbed magnetic fields of Cases 0, 1 and 2.

lines. An electron orbit confined within the magnetic island is highlighted in red, and two orbits approximately following unperturbed magnetic field lines are highlighted in black. In Fig. 5(b) we show Poincaré sections of orbits of three FO 10 MeV RE moving in the magnetic field of Case 0. Their initial pitch-angle is $\vartheta_0 = 0°$, these RE have been followed by approximately 300 $\mu$s. We notice that due to the spatial variation of the magnetic field, the pitch angle of these RE varies along their orbits, e.g. see Fig. 5 of Ref. 15, and therefore their $r_L$ varies, too. This variation of $\vartheta$ increases with energy and with the initial pitch angle $\vartheta_0$. The Poincaré sections of panel (b) seem distorted with respect to those of panel (a) due to the drifts of the RE orbits, but island-like structures and well-formed closed surfaces described by RE orbits are clearly visible. We highlight in red and black the RE orbits with the same initial positions than those highlighted in panel (a). In panel (c) of the same figure we show the corresponding Poincaré sections of 10 MeV RE orbits with initial pitch angle of $\vartheta_0 = 40°$, their initial positions are the same as for panel (b), the only difference in this simulation is that we effectively increased the initial RE Larmor radius. For 10 MeV RE with $\vartheta_0 = 40°$ the characteristic Larmor radius in the simulated magnetic field is $r_L \approx 0.011$ m (black star in Fig 4), this means $r_L \sim \delta r_{21}$. We highlight in red the orbit with the same initial position than the red orbits of panels (a) and (b). As it can be seen from Fig 5(c), the red orbit no longer remain confined, this became untrapped, exploring thick radial regions of the plasma without restrictions along the poloidal direction $\theta$. This behaviour of exploring thick radial regions of the plasma without restrictions along $\theta$ is the typical behaviour for high-energy RE with large $r_L$ moving in unperturbed magnetic field lines (highlighted in black). In this sense, we find that when $r_L \gtrsim r_{mn}$, the orbits of the simulated FO RE are similar to those of RE moving in unperturbed magnetic fields, averaging the effects of the magnetic perturbation. Only when $r_L < r_{mn}$, FO orbits initially well confined within a magnetic island remain trapped within island-like structures. It is important to mention that the existence of thick radial regions described by the RE orbits on these Poincaré sections is due to their finite $r_L$, not because the orbits are stochastic.

In Fig. 5(d) we show a one-to-one comparison between Poincaré sections of FO (red dots showing orbits of panel (b)) and GC (blue dots) orbits of 10 MeV RE with $\vartheta_0 = 0°$. As it can be seen, for this energy and pitch-angle FO and GC orbits are practically the same. The initial conditions in both FO and GC simulations are identical. We perform the same one-to-one comparison between FO (same as panel (c)) and GC orbits of 10 MeV RE with $\vartheta_0 = 40°$ in Fig. 5(e). Now, a striking difference is found: GC orbits describe shifted, well-defined flux surfaces and a trapped orbit in the magnetic island, while FO orbits explore thick radial regions showing no confinement due to the magnetic island. As suspected, GC simulations can not capture FLR effects that cause RE to become untrapped from the magnetic islands. In Fig. 5(f) we compare the GC orbits of panels (d) and (e), as it can be seen, the only visible effect from varying the pitch-angle (magnetic moment) is to modify the size of the island described by GC orbits.

We also study the dynamics of FO 25 MeV RE orbits with $\vartheta_0 = 0°$ and $\vartheta_0 = 15°$ in Fig. 5(g) and (h), respectively. As before, the red and black highlighted orbits correspond to the highlighted orbits of Fig. 5(a). The effect of increasing the initial pitch-angle to $\vartheta_0 = 15°$ is to make $r_L \sim \delta r_{21}$ (black circle in Fig. 4). As for the case of FO 10 MeV RE, when the Larmor radius is similar to the half-width of the magnetic island, the RE that were initially confined within the island for small pitch-angles, become untrapped, exploring thick radial regions of the plasma. Fig. 5(i) and (j) show the corresponding comparison between FO (red dots) and GC (blue dots) orbits. Once more, GC orbits predict regular RE orbits similar to RE with small pitch-angles (panels (g) and (i)), while FO orbits exhibit a more complex dynamics of RE that become untrapped once that $r_L \sim \delta r_{21}$.

## VI. EFFECT OF STOCHASTICITY ON RE TRANSPORT

A good understanding of RE confinement in perturbed magnetic fields is of particular interest if instabilities are to be used as a mechanism for avoidance or mitigation of RE in current and future tokamak experiments[9]. In this section we study the effect of magnetic field stochasticity on RE confinement. We simulate FO and GC RE with different energies in magnetic fields with different levels of stochasticity and measure the variations on the RE confinement.

First, we study the fast-timescale RE transport driven

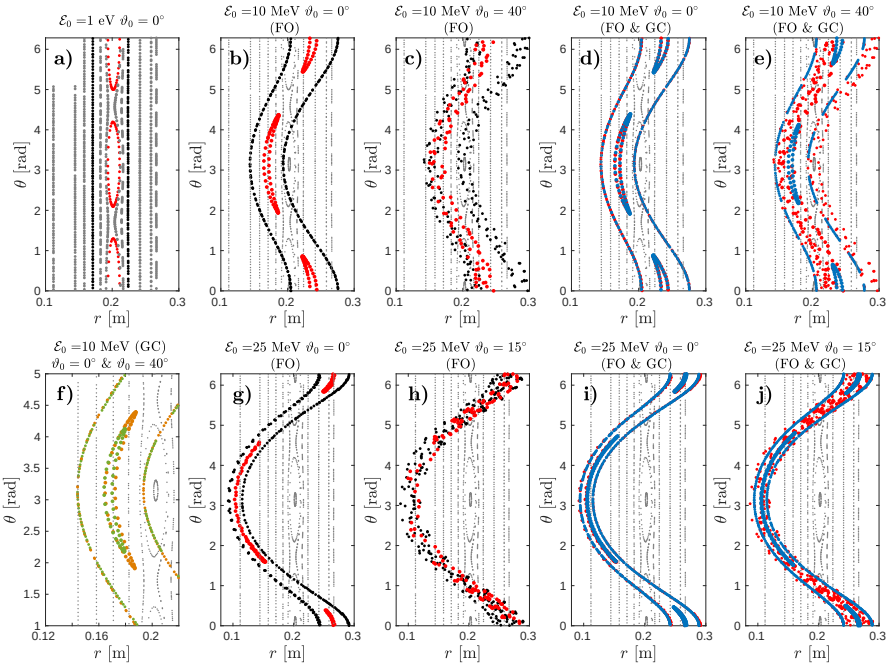


FIG. 5. Poincaré sections of RE orbits in the perturbed magnetic field of Case 0. Panel a): Poincaré sections of 1 eV electron orbits streaming along the perturbed magnetic field. One orbit confined within the magnetic island of the $(m, n) = (2, 1)$ mode is highlighted in red. Two other non-confined orbits are highlighted in black. Panel b): Poincaré sections of three FO 10 MeV electrons orbits with the same initial spatial condition and pitch-angle ($\vartheta_0 = 0°$) as those highlighted in panel (a). The orbits look distorted due to the large drifts of the RE. For comparison, we show with gray small dots the Poincaré sections of panel (a). Panel c) Same as panel (b), but for 10 MeV RE with $\vartheta_0 = 40°$. Their Larmor radius is so that $r_L \sim \delta r_{21}$, see star in Fig. 4. Panel d): Comparison between the FO (red dots) and GC (blue dots) Poincaré sections of 10 MeV RE with $\vartheta_0 = 0°$. The initial condition of GC particles are equivalent to that of FO particles, see Appendix A for details. Panel e): Same as panel (d) for 10 MeV with $\vartheta_0 = 40°$. Panel d): Comparison of GC 10 MeV RE orbits with $\vartheta = 0°$ (orange) and $\vartheta = 40°$ (green). Panel g): Same as panel (b) for 25 MeV. Panel h): Same as panel (c) for 25 MeV with $\vartheta = 15°$. Their Larmor radius is so that $r_L \sim \delta r_{21}$, see circle in Fig. 4. Panel i): Same as panel (d) for 25 MeV. Panel j): Same as panel (e) for 25 MeV with $\vartheta = 15°$.

by drifts in non-perturbed magnetic fields, that is, prompt RE losses that occur within $t \sim 1$ $\mu s$ . We compare FO and GC simulations to show how full-orbit effects can modify the RE confinement in these scenarios. Then, we repeat the analysis including the perturbations of Case 1 and 2 of Sec. II to measure the change in RE confinement with respect to prompt losses.

### A. Runaways prompt losses in non-perturbed magnetic fields

We start by studying fast-timescale RE transport due to orbit drifts and FO effects. For this, we evolve ensembles of RE in the non-perturbed magnetic field of Eq. (1). Initially, the RE are uniformly distributed in a torus of radius $r = a$, centered at the magnetic axis $R_0$. Here, $a$ is the radius of the plasma of Eq. (2). We use five values for the initial pitch-angle of the simulated RE, $\vartheta_0 = 5°$, 10°, 20°, 30°, and 40°. The initial gyro-phases of the FO RE are random. The initial energies of the RE are set to $\mathcal{E}_0 = 1$ MeV, 10 MeV, and 25 MeV. The simulation time is set to 0.4 ms for 1 MeV RE and to 1 ms for 10 MeV and 25 MeV RE. The shorter simulation time for 1 MeV RE is due to computational constrains. However, prompt losses occur in a time scale of about $t \sim 1\mu$s. After this short timescale we observe that the number of confined RE after promtp losses $N_{PL}$ has reached a saturated value. Here, we say that a RE is confined if it is within the last closed flux surface (LCFS) at $r = a$. To have a better

idea about the timescales involved in the problem, RE perform a toroidal transit in approximately $3 \times 10^{-8}$ s, the bounce period or poloidal transit time around $q = 2$ is $8 \times 10^{-8}$, the fast gyro-period of 1 MeV RE is about $5 \times 10^{-11}$ and $9 \times 10^{-10}$ for 25 MeV RE. The number of simulated particles is set to $N_{sim} = 100,000$, and the MC standard error of $N_{PL}/N_{sim}$ is $\epsilon_{N_{PL}/N_{sim}} \sim 0.25$ %.

In Fig. 6 we show $N_{PL}$ as a fraction of the number of simulated RE $N_{sim}$ by the end of each simulation for three sets of initial conditions for FO and GC simulations: blue and grey circles show $N_{PL}/N_{sim}$ for FO and GC simulations of 1 MeV RE. Red and grey squares in Fig. 6 show $N_{PL}/N_{sim}$ for FO and GC 10 MeV RE. Similarly, green and grey stars show $N_{PL}/N_{sim}$ for FO and GC 25 MeV, respectively. As it can be seen, prompt losses increase with increasing values of $\mathcal{E}_0$ and $\vartheta_0$. $N_{PL}/N_{sim}$ decreases, from around 90% for 1 MeV RE to about 40% for 25 MeV RE, respectively. This is consistent with the idea that by increasing the energy of the RE the $\nabla B$ drift ($\sim v_\perp^2 \boldsymbol{B} \times \nabla B$), and curvature drifts ($\sim v_\parallel^2 \boldsymbol{B} \times \boldsymbol{R}$ in vacuum fields) increase, too. A larger drift allows RE to cross more magnetic surfaces along their orbits (e.g. Fig. 5(b) and (g)), and eventually leave the plasma. GC simulations also predict the same energy and pitch-angle dependence of $N_{PL}$, but is less visible than for FO simulations. Notice the drop in $N_{PL}$ as we increase the initial pitch angle $\vartheta_0$ from 5° to 40° in FO simulations. This weak dependence of $N_{PL}$ on the pitch-angle might be because the $\nabla B$ drift and curvature drifts tend to compensate for their effects on RE confinement when $\vartheta_0$ increases: the $\nabla B$ drift effects becoming stronger with increasing $\vartheta_0$, while curvature drift effects weaken with increasing $\vartheta_0$.

The differences in the values of $N_{PL}$ between FO and GC simulations are explained to a good degree by FLR effects. In Fig. 7(a) we show the initial position on the poloidal plane of the FO RE with $\vartheta_0 = 40°$ of Fig. 6 that remained confined by the end of the simulation. Grey dots represent 1 MeV RE, and blue and orange dots represent 10 MeV and 25 MeV RE, respectively. Colored dots overlap, meaning that we find blue dots behind the orange dots, and grey dots behind the orange and blue dots. As mentioned before, as the RE energy is increased the drifts become larger, shifting the RE orbits towards the LFS. We can find quantitatively where the differences in $N_{PL}$ between FO and GC simulations arise by binning the positions of the RE of Fig. 7(a) for FO and GC simulations, $N_{PL}^{FO}(R,Z)$ and $N_{PL}^{GC}(R,Z)$ respectively, and then calculating the difference $N_{PL}^{FO}(R,Z) - N_{PL}^{GC}(R,Z)$. This is shown in Fig. 7(b) for 10 MeV RE. Similar results are found for 1 MeV and 25 MeV RE. We observe some fluctuations of about ±30 particles per bin in the central region spanned by the blue dots in panel (a). These fluctuations are MC fluctuations due to the small differences between the initial spatial conditions in the FO and GC simulations. Larger values of $N_{PL}^{FO}(R,Z) - N_{PL}^{GC}(R,Z) \sim -100$ particles per bin, are found at the edge of the region spanned by the blue dots in panel (a). These negative values represent RE that remain confined in the GC simulations, but are lost in FO simulations when crossing the LCFS (thick black circle) due to their FLR.

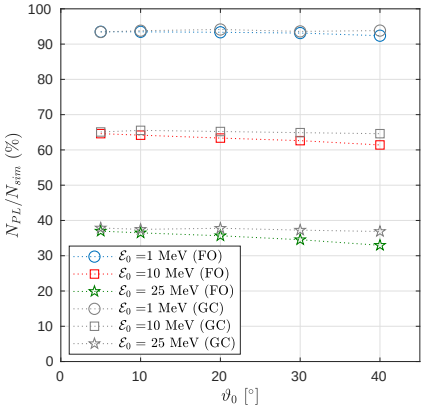


FIG. 6. Number of confined RE $N_{PL}$ in the non-perturbed magnetic field of Eq. (1). The blue and grey circles show $N_{PL}$ as a fraction of $N_{sim}$ for FO and GC 1 MeV RE by the end of the simulation. Red and black squares show the corresponding $N_{PL}$ for FO and GC 10 MeV RE. Green and grey stars show the corresponding $N_{PL}$ for FO and GC 25 MeV RE. Prompt losses increase ($N_{PL}$ decreases) as we increase the RE energy, this due to drift orbit effects. FO and GC simulations show good agreement for small pitch angles. FO effects start to be noticeable at large energies and large pitch-angles. The number of simulated particles is set to $N_{sim} = 100,000$, and the MC standard error of $N_{PL}/N_{sim}$ is $\epsilon_{N_{PL}/N_{sim}} \sim 0.25$ %.

Summarizing, RE prompt losses in non-perturbed magnetic fields are mainly due to $\nabla B$ and curvature drifts that occur in fast timescales of about 1 $mu$s. These prompt losses increase as we increase the RE energy and pitch-angle. In general, GC and FO simulations show a good agreement in trends and values, showing small differences in the RE confinement near the LCFS caused by FLR effects.

### B. Effects of magnetic field stochasticity on RE confinement

We now study the confinement properties of RE in the perturbed magnetic fields of Sec. II. The RE initial energies, pitch-angles, spatial conditions, gyro-phases, and simulation times are the same as in the simulations of Sec. VI A. It is only $N_{sim}$ that is varied as reported in each case.

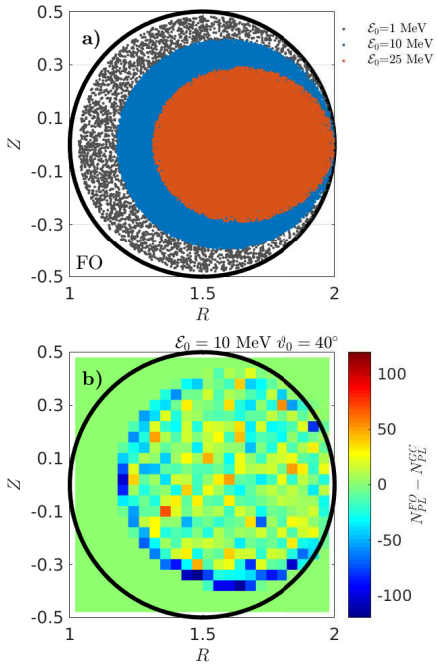


FIG. 7. Panel a): Initial position on the $RZ$ plane of simulated RE that remained confined by the end of FO simulations of Fig. 6. The initial pitch-angle is $\vartheta_0 = 40°$ for all cases. Grey dots represent 1 MeV RE, and blue and orange dots represent 10 MeV and 25 RE, respectively. Colored dots overlap, meaning that we find blue dots behind the orange dots, and grey dots behind the orange and blue dots. Panel b): computed values of $N_{PL}^{FO}(R,Z) - N_{PL}^{GC}(R,Z)$ as explained in the main text. The number of simulation particles is set to $N_{sim} = 10,000$ for 1 MeV RE, and $N_{sim} = 100,000$ for 10 MeV and 25 MeV RE.

In order to isolate and quantitatively measure the effect of magnetic stochasticity on RE confinement, we define the RE loss coefficient $L_{RE}$ as follows:

$$L_{RE}(N_{PL}, N) = 100 \times \left( \frac{N_{PL} - N}{N_{PL}} \right) . \qquad (10)$$

Here, $N_{PL}$ is the number of confined particles that remained confined by the end of the simulations of Sec. VI A for a given energy and pitch-angle, and $N$ is the number of RE that remain confined by the end of the new simulations with perturbed magnetic fields. The MC standard error of $L_{RE}$ is approximated as $\epsilon_{L_{RE}} \approx |L_{RE}(N_{PL}, N + \epsilon_N) - L_{RE}(N_{PL}, N)|$. In Fig, 8(a) we show the time evolution of the number of confined 1 MeV RE , $N/N_{sim}$, in the simulation with the perturbed magnetic field of Case 1. Solid (dashed) lines show $N/N_{sim}$ vs. time for FO (GC) RE with various $\vartheta_0$. The number of simulated particles was set to $N_{sim} = 1,000$ for these simulations, thus the MC standard error in $N/N_{sim}$ is $\epsilon_{N/N_{sim}} \sim 2\%$, see Fig. 3. As it can be seen from this figure, at early times there is a drop in $N/N_{sim}$ due to prompt losses, after this the number of confined RE remain unchanged for both FO and GC simulations. Similarly, in Fig, 8(b) we show the time evolution of $N/N_{sim}$ for the simulations using the perturbed magnetic field of Case 2, that is, the magnetic field with wide stochastic regions. The number of simulated particles is set to $N_{sim} = 10,000$. This time, $N/N_{sim}$ does not saturate after the rapid prompt losses at early times, showing larger RE losses in the case of GC simulations. Fig. 8(c) and (d) show the corresponding time evolution for 25 MeV evolving in the perturbed magnetic fields of Case 1 (panel (c)) and Case 2 (panel (d)). The qualitative behaviour is the same as for the simulations of 1 MeV RE, but prompt losses are larger as showed in Sec. VI A.

In Fig. 9 we now isolate the effect of magnetic stochasticity by computing $L_{RE}$ at the end of the simulations of Fig. 8. We observe no further RE losses ($L_{RE} \approx 0$) with respect to prompt losses for both FO and GC simulations of 1 MeV in the magnetic fields of Case 1. However, for simulations using the magnetic field of Case 2 we observe $L_{RE} \sim 30\%$ for FO simulations, and $L_{RE} \sim 60\%$ for GC simulations. We note that these RE losses occur in a finite time ($t = 0.4$ ms), and might look different in very long times. However, these long time scales are not in the scope of the present work. In a similar way, FO and GC simulations of 25 MeV RE in the magnetic field of Case 1 show no further losses with respect to prompt losses. It is for the stochastic fields of Case 2 that we observe few particle losses $L_{RE} \sim 8\%$ for FO RE with $\vartheta_0 = 5°$ and $10°$ and no further losses (within error bars) for larger $\vartheta_0$. On the other hand, GC simulations predict large losses in this case for all pitch-angles, $L_{RE} \sim 30\%$. As in the case of 1 MeV RE, these RE losses occur in a finite time ($t = 1$ ms), and might look different in very long time scales. These results have been corroborated by reducing the time step by one order of magnitude in the GC simulations, this provides better convergence and energy conservation, see Appendix A. In order to investigate the cause of these differences between FO and GC simulations we analyze the density profiles of simulated particles in each case, this is shown in Fig. 10 for 1 MeV RE and in Fig. 11 for 25 MeV. We calculate these density profiles on the $RZ$ plane, $N(R,Z)$, by binning the position of the RE at the end of each simulation. In Fig. 10(a) we show $N(R,Z)$ for FO 1 MeV RE with $\vartheta_0 = 40°$ and Fig. 10(b) shows $N(R,Z)$ for the corresponding GC simulation. Clearly, the main difference in $N(R,Z)$ between FO and GC simulations is found for the plasma region with $r \geq 0.325$ m, which corresponds to the stochastic region where modes $m = 3$ to $m = 6$ overlap (see Fig. 1(c) and (d)). For guidance, Fig. 10(c) shows Poincaré sec-

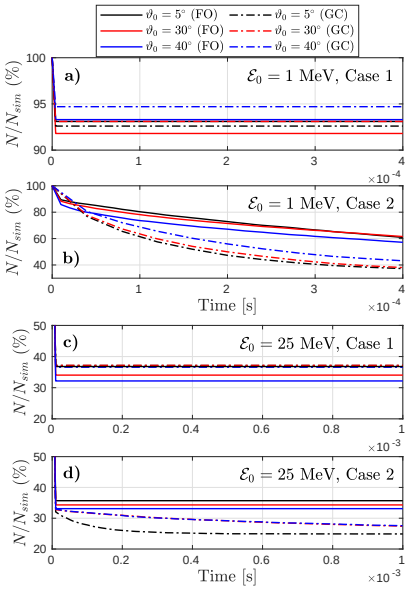


FIG. 8. Number of confined particles $N$ as function of time. Panel a): Number of confined particles $N$ as a fraction of $N_{sim}$ for FO (solid lines) and GC (dash-dot lines) 1 MeV RE. Various values of $\vartheta_0$ are shown. Both FO and GC simulations do not show losses after the fast prompt losses at the beginning of the simulations, $t \sim 1\mu$s. Panel b): Same as panel (a) for 1 MeV RE evolving in the magnetic fields of Case 2. A slow decay of $N$ is observed for both FO and GC simulations. However, more RE are lost in GC simulations. Panel c): Same as panel (a) for 25 MeV. No RE losses are observed after the prompt losses at $t \sim 1\mu$s. Panel d): Same as panel (c) for 25 MeV evolving in the magnetic field of Case 2. While FO simulations do not show RE losses after the prompt losses, GC simulations show relatively, large RE losses occurring during the entire simulation.

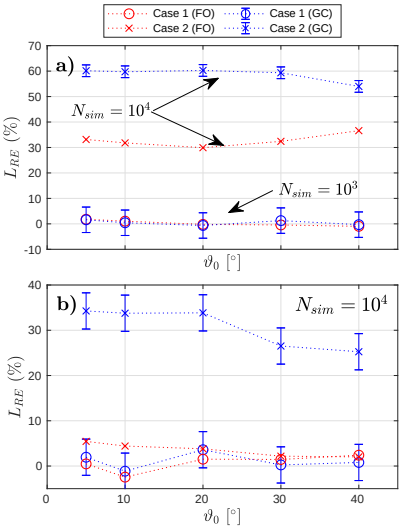


FIG. 9. RE losses due to stochasticity of the magnetic field. Panel a): RE loss coefficient of Eq. (10) for 1 MeV FO (red markers) and GC (blue markers) RE simulated in the perturbed magnetic fields of Case 1 (○ markers) and Case 2 (× markers). No RE losses are observed after the prompt losses ($L_{RE} \sim 0$) for the perturbed magnetic field of Case 1. In contrast, for the perturbed magnetic field of Case 2, the stochasticity of the magnetic field produces considerable RE losses. GC simulations show almost two times the RE losses ($L_{RE} \sim 60$ %) predicted by FO simulations ($L_{RE} \sim 30$ %). We have used $N_{sim} = 1,000$ for FO and GC simulations of RE in the magnetic fields of Case 1, and $N_{sim} = 10,000$ for FO and GC simulations using the magnetic field of Case 2. We show $\epsilon_{L_{RE}}$ with error bars for some simulations. Panel b): Same as panel (a) for 25 MeV RE. In this case, FO and GC simulations show no RE losses in the magnetic field of Case 1. For RE evolving in the fields of Case 2 only GC simulations show RE losses due to the stochastic fields of Case 2 (blue crosses). In all these simulations $N_{sim} = 10,000$.

tions of 1 MeV RE with $\vartheta_0 = 0°$, we highlight islands $m = 2$ in blue, $m = 3$ in yellow and $m = 4$ in green. We note that these are not magnetic islands, but island-like structures described by RE orbits. The magenta bold circle has a radius of $r = 0.325$ m, and approximately separates the regions where FO and GC shows similar results (inner region), and large differences in $N(R, Z)$ (outer region). Similar results are found for other initial pitch-angles. The LCFS is highlighted with a bold grey circle at $r = a$ in all panels.

In the same way, In Fig. 11(a) we show $N(R, Z)$ for a FO simulation of 25 MeV RE with $\vartheta_0 = 40°$, and $N(R, Z)$ for the corresponding GC simulation in Fig. 11(b). The bold magenta circle, centered at $R = 1.64$ and having a radius $r = 0.25$ roughly separates the regions where FO and GC simulations show similar results (inner region), and differente results (outer region). As for the case of 1 MeV, this circle seems to lay between the islands with $m = 3$ and $m = 4$. We note that these are not magnetic islands, but island-like structures described by RE orbits. In Fig. 11(c) we show Poincaré sections of 25 MeV RE with $\vartheta_0 = 0°$, we highlight the island with $m = 2$ in blue, $m = 3$ in yellow, and $m = 4$ in green.

From our analysis, we observe that GC and FO simulations predict basically the same prompt losses in non-perturbed magnetic fields. However, GC simulations predict more RE losses than FO simulations using stochas-

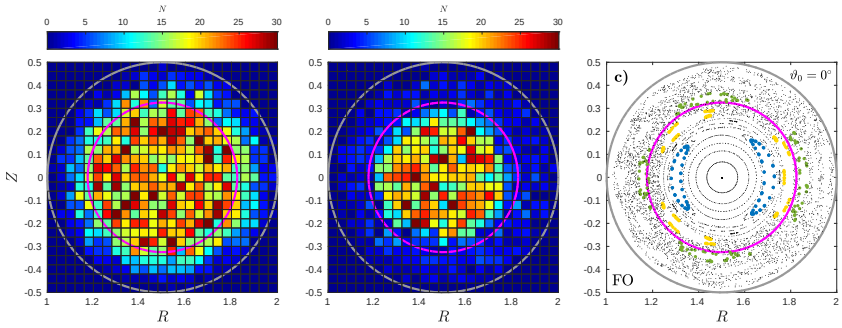


FIG. 10. RE density profiles on the $RZ$ plane of simulated 1 MeV RE. Panel a): A binning of the position on the $RZ$ plane number of simulated FO RE in the magnetic fields of Case 2 at $t = 0.4$ ms, see Fig. 8(b). The pitch-angle of these RE is $\vartheta = 40°$. The grey bold circle shows the LCFS at $r = a$. The magenta circle is centered at the magnetic axis ($R_0$) and with radius $r = 0.325$ m, shows the region between the modes $m = 3$ and $m = 4$, where stochasticity of the magnetic field is predicted by the Chirikov parameter (Fig. 2). Panel b): Same as panel (a) for the corresponding GC simulation of 1 MeV RE at $t = 0.4$ ms. The main difference between the FO and GC simulation is observed for $r > 0.325$ m, which corresponds to the stochastic region of the magnetic field of Case 2. Panel c): Poincare sections of 1 MeV RE with $\vartheta_0 = 0°$. We highlight the islands seen by RE orbits corresponding to $m = 2, 3$, and 4.

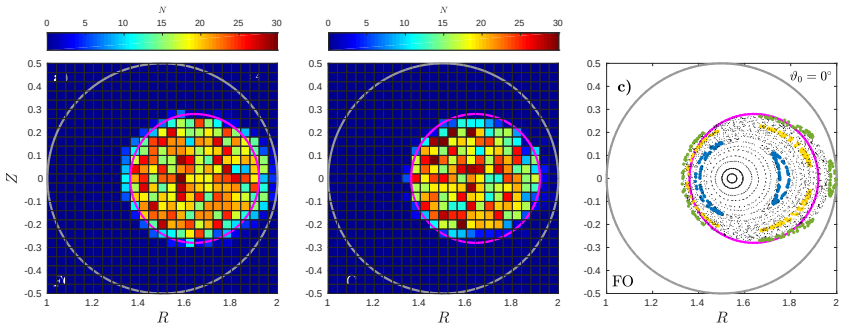


FIG. 11. RE density profiles on the $RZ$ plane of simulated 25 MeV RE. Panel a): Same as panel (a) of Fig. 10 for 25 MeV at $t = 1$ ms. The magenta circle in this case is centered at $R = 1.64$ and has a radius of $r = 0.25$ m. Panel b): Same as panel (b) of Fig. 10 for GC 25 MeV at $t = 1$ ms. Panel c): Poincaré sections of FO 25 MeV RE orbits with $\vartheta_0 = 0°$. Only a small stochastic region is observed beyond the $m = 3$ structure shown by the RE orbits (yellow dots).

tic magnetic fields. For the first time this difference is quantified. GC simulations doubles the value of $L_{RE}$ of FO simulations of 1 MeV RE, while $L_{RE}$ is almost four times larger for GC simulations of 25 MeV RE with respect to the corresponding FO simulations. As reported in Refs. 11 and 12, GC orbits resemble the structure of the magnetic field, following stochastic orbits that eventually leave the plasma. We find that FO effects delay these losses, see Fig. 8(b) and (d), enhancing RE confinement. Possibly, the same FO effects observed in Sec. V might produce this delay.

Regarding the relationship between the Chirikov parameter $S_{m_1 m_2}$ of Eq. (7) and its heuristic extension $\hat{S}_{m_1 m_2}$ of Eq. (8) with the RE confinement studied in this section: we observe that $S_{m_1 m_2}$ is a good indicator of the trends in $L_{RE}$, that is, when $S_{m_1 m_2} > 1$ we observe

$L_{RE} > 0$ for both FO and GC simulations. The heuristic extension of the Chirikov parameter $\hat{S}_{m_1 m_2}$ does not seem to hold, actually it shows the opposite trend of FO simulations. Therefore, the ansatz of RE with a finite $r_L$ interacting with two adjacent magnetic islands does not hold for the scenarios studied in this work. This suggests that a more detailed derivation of the Chirikov parameter for RE orbits is needed. We anticipate that such derivation might require to solve the complex dynamics of RE orbits in the 6-D phase space to find the position of the island-like structures described by the orbits and see when they overlap. We also note that FO effects can make it challenging to find such island-like structures.

## VII. EFFECT OF TOROIDAL ROTATION ON RE TRANSPORT

Finally, we study the effect of toroidal rotation of $\delta \boldsymbol{B}_{mn}$ on RE confinement. The occurrence of low-frequency MHD-like modes has been observed in experiments and simulations of tokamak plasmas where RE are present[11,25]. Despite the fact that we can set the rotation frequency of $\delta \boldsymbol{B}_{mn}$ to arbitrary values, we will focus our study to the low-frequency cases since our analytical model for $\delta \boldsymbol{B}_{mn}$ captures well the general structure of low-frequency MHD-like modes, but not necessarily the structure of high-frequency modes such as whistler waves, where wave-particle interactions might occur[6–8].

In all the simulations of this section we set the toroidal rotation frequency to $f = 50$ kHz, which corresponds to an angular rotation frequency $\omega_{mn} \sim 300$ kHz, producing an inductive electric field with maximum amplitude of up to $E \approx 6$ V/m. For the plasma parameters used in this work, the relativistic electron cyclotron frequency is $\Omega_{RE} \sim 10$ GHz, and the bounce frequency of the RE at $q = 2$ is $\omega_b \sim 100$ MHz. These frequencies are much larger than $\omega_{mn}$. We note that this value of $\omega_{mn}$ is not representative of all the scenarios where RE occur in rotation perturbed magnetic fields, but it is a value that can be found in the literature for a medium-size tokamak where RE with several MeV were observed[25].

Since in Sec. VI B it was shown that FO effects are important in the study of RE transport in perturbed magnetic fields, we only use FO simulations in this section.

### A. RE transport in the presence of a rotating magnetic island

First, we repeat the analysis of Sec. V of the RE dynamics around the magnetic island of Case 0, but this time adding toroidal rotation and the resulting inductive electric field of Eq. (6). In Fig. 12(a) we show Poincaré sections of 1 eV electron orbits along the perturbed magnetic field of Case 0. We also show the toroidal component of the inductive electric field of Eq. (8) at $t = 0$. As it can be seen, there are intense regions of $|E_\zeta| \approx 6$ V/m within the magnetic islands. In all our simulations, the radial $E_r$ and poloidal $E_\theta$ components of $\boldsymbol{E}$ are about two orders of magnitude smaller than $E_\zeta$. Fig. 12(b) shows Poincaré sections of FO 10 MeV RE with $\vartheta_0 = 0°$. **These Poincaré sections are calculated in the laboratory frame of reference, as in the case of non-rotating magnetic fields**. The simulation time is set to $t = 300$ $\mu$s. As in the case with no rotation, RE orbits show distorted with respect to magnetic field surfaces, this due to particle drifts. RE initially not trapped in the island (black dots) do not show a visible difference with respect to the case with no rotation. However, the RE orbit initially trapped in the magnetic island (red dots) seems to be transported within the island, co-rotating clockwise on the poloidal plane. Fig. 12(c) shows the corresponding Poincaré sections of FO 10 MeV with $\vartheta_0 = 40°$, so that $r_L \sim \delta r_{21}$. **These Poincaré sections are calculated in the laboratory frame of reference**. As in the simulations with no rotation, RE orbits explore thick radial regions of the plasma, not being trapped by the magnetic island, see Fig. 5(c). In these simulations the mean energy of the RE remains almost constant, with small fluctuations of up to 100 keV. This is due to the relatively high bounce frequency of these RE, that averages the effects of the regions of large positive and negative electric fields, c.f. Fig. 12(a).

### B. Effect of toroidal rotation on RE confinement in stochastic magnetic fields

Now, we study the effect of toroidal rotation on RE confinement in the stochastic fields of Case 2. We perform two FO simulations of RE with initial energy of 1 MeV and 25 MeV. The initial spatial condition, gyrophases, and pitch-angles are the same as in the simulations of Sec. VI A, that is, the RE are uniformly distributed in a torus of radius $r = a$, centered at the magnetic axis $R_0$. We use five values for the initial pitch-angle of the simulated RE, $\vartheta_0 = 5°$, $10°$, $20°$, $30°$, and $40°$. The initial gyro-phases of the FO RE are random. The simulation time is set to $t = 0.1$ ms in both simulations.

As in Sec. VI B, we compute $L_{RE}$ by the end of each simulation. In Fig. 13(a) we show $L_{RE}$ with filled magenta squares for the simulation of 1 MeV RE. For comparison, we also show the corresponding $L_{RE}$ at $t = 0.1$ ms for the simulation with no rotation (green stars) of Fig. 9(a). No difference between simulations with and without rotation is found. Similarly, in Fig. 13(b) we show $L_{RE}$ for the simulation of 25 MeV with rotation (filled magneta squares) and without rotation (green starts). As for 1 MeV RE, we do not observe any effect of rotation on RE confinement. The same qualitative results are found if the toroidal rotation is set to be counter-clockwise ($\omega_{mn} = -300$ kHz).

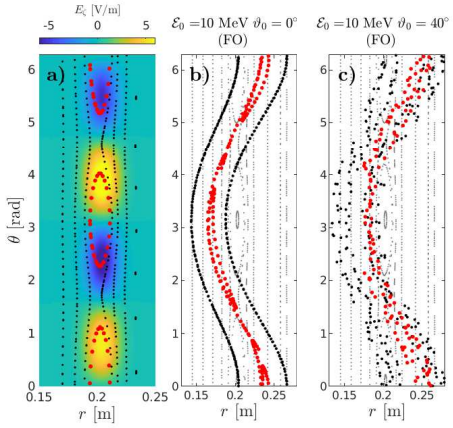


FIG. 12. Poincaré sections of RE in the perturbed, rotating magnetic field of Case 1. Panel a): Poincaré sections of 1 eV electrons streaming along the perturbed magnetic field. One orbit confined within the magnetic island of the $(m, n) = (2, 1)$ mode is highlighted in red. The toroidal component of the inductive electric field at $t = 0$ is shown, too. Panel b): Poincaré sections of 10 MeV electrons with initial $\vartheta_0 = 0°$. The red orbit, corresponding to the same initial position as the red orbit of panel (a), still shows a topology of a distorted island that moves along the poloidal direction as function of time. Non-confined orbits (black dots) do not show any difference with respect to non-rotating fields, e.g. Fig. 5(b). Panel c): same as panel (b), but for 10 MeV electrons with $\vartheta_0 = 40°$. For these RE $r_L \sim \delta r_{21}$. Their orbits resemble those of RE in non-rotating fields, see Fig. 5(c).

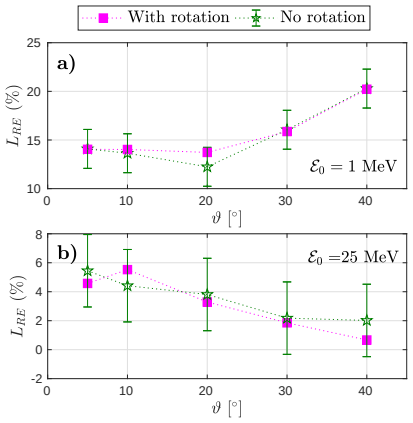


FIG. 13. RE losses due to toroidal rotation of the magnetic perturbations of Case 2. Panel a): $L_{RE}$ for FO 1 MeV RE with $\vartheta_0 = 5°, 10°, 20°, 30°$, and $\vartheta = 40°$. he green stars (magenta solid squares) show $L_{RE}$ for the simulation without (with) rotation. The simulation parameters are the same as in the simulations of Fig. 6, the simulation time is set to $t = 0.1$ ms. No RE losses are observed with respect to non-rotating perturbed fields. Panel b): same as panel (a) for 25 MeV. As for 1 MeV RE, no losses are observed due to toroidal rotation.

## VIII. DISCUSSION

In this work we studied the dynamics of full-orbit (FO) and guiding-center (GC) runaway electrons with various energies and pitch-angles evolving in perturbed magnetic fields. We used KORC for simulating FO and GC RE in the equilibrium magnetic field of Refs. 14 and 15 that include MHD-like modes[22,23]. Despite the fact that our analytical model for the magnetic field is simple, it captures most of the important effects on the RE dynamics evolving in toroidal configurations. No collisional effects or radiation losses were included in our simulations, since these effects have little effect on RE dynamics in the studied time scales ($t \sim 1$ ms).

Our study sheds new light into the confinement and transport of RE in perturbed magnetic fields that exhibit stochasticity. This is of particular importance for the generation of avoidance and/or mitigation mechanisms of RE in current and future tokamak experiments.

In Sec. V we studied RE transport in the presence of a magnetic island. We performed FO and GC simulations of RE evolving in the magnetic field of Case 0. FO and GC simulations showed that despite the fact that RE have large orbit drifts, RE orbits display island-like structures that resemble magnetic islands when the RE Larmor radius is small. When $r_L$ became comparable to the half-width of the magnetic island $\delta r$, FO simulations showed that RE initially trapped within the island-like structures became untrapped, exploring thick radial regions of the plasma in the same way as RE moving in non-perturbed magnetic fields do. Contrary, GC simulations continued to predict trapped RE orbits within island-like structures. This suggest that FO effects cause the averaging of magnetic perturbations when $r_L \sim \delta r$.

In Sec. VI we studied the confinement of low-energy (1 MeV) and high-energy (25 MeV) RE in stochastic magnetic fields. In order to separate fast-timescale transport (prompt losses) driven mainly by drift orbit effects from relatively long-timescale ($t \sim 1$ ms) transport due to magnetic field stochasticity, we first calculated prompt losses of RE in non-perturbed magnetic fields, see Sec. VI A. In general, both FO and GC simulations predicted similar prompt losses, see Fig. 6. Then, we included magnetic perturbations in our FO and GC simulations to measure the RE losses with respect to prompt losses, $L_{RE}$ of Eq. (10). Both FO and GC simulations exhibited less particle losses for high-energy RE than for low-energy RE, see Fig. 9. This trends have been ob-

served experimentally and in previous numerical studies following GC particles[11,16–18]. However, our one-to-one comparison between FO and GC simulations allowed us to quantitatively measure FO effects on these scenarios: it is found that GC predictions of $L_{RE}$ are twice the predictions of FO simulations for 1 MeV RE, and four times those of FO simulations for 25 MeV RE. One possible explanation for this is that FO effects might gyro-average magnetic field stochasticity, delaying RE losses, while as suggested in Refs. 11 and 12, GC orbits follow more closely magnetic field lines, allowing the RE to leave the plasma more quickly as they follow open field lines. Comparison of density profiles on the $RZ$ plane, confirmed that the main differences between FO and GC simulations arise in the stochastic regions of the magnetic field, see Figs. 10 and 11. Regarding the relationship between magnetic field stochasticity predicted by the Chirikov parameter $S_{m_1m_2}$ and RE transport, we found that $S_{m_1m_2}$ is a good indicator of the trends in $L_{RE}$, that is, when $S_{m_1m_2} > 1$ we observed $L_{RE} > 0$ for both FO and GC simulations. On the other hand, the heuristic extension of the Chirikov parameter $\hat{S}_{m_1m_2}$ does not seem to hold, showing opposite trends with respect to FO simulations, that is, $\hat{S}_{m_1m_2}$ becoming larger as $r_L$ increases, while $L_{RE}$ decreases for FO simulations with larger $r_L$. We note that the observed RE transport in stochastic magnetic fields occur in a finite time ($t \sim 1$), and might look different in very long times ($t \gg 1$ ms). However, the latter time scales are not in the scope of the present work.

Finally, in Sec. VII we studied RE transport including FO effects, magnetic field stochasticity and toroidal rotation. For the scenarios considered in this work we do not see important differences between simulations with and without rotation. We found that RE with $r_L < \delta r$ are transported within magnetic islands as they rotate, see Fig. 12(b). On the other hand, RE with $r_L \sim \delta r$ behave similar to RE moving in magnetic fields without rotation. FO simulations of RE evolving in rotating, stochastic magnetic fields did not exhibit differences with respect to simulations with no rotation, see Fig. 13. The mean RE energy remained practically unchanged in these simulations. This, due to the rapid averaging of the positive and negatives regions of the electric field as the RE stream along the magnetic field. Only fluctuations of up to 100 keV in the RE energy are observed.

It is important to mention that studying RE transport in scenarios relevant to the thermal and/or current quench in disrupting plasmas are out of the scope of this work. A consistent study in those scenarios would require the inclusion of the exact mode structure of the magnetic perturbations, as well as other effects as the plasma shape, impurities, radiation losses, and self-consistent electric fields.

Our results answer the long-standing question of when FO effects need to be included when studying RE transport in perturbed toroidal magnetic fields, and quantify the difference between FO and GC predictions of RE losses in stochastic magnetic fields.

Future work might include the use of external magnetic fields from reconstructions and/or numerical simulations that contains the exact mode structure in plasmas where avoidance or mitigation mechanisms are to be developed.

## ACKNOWLEDGMENTS

This work was partially funded by the National Autonomous University of Mexico (UNAM) through the PAPIIT project IN112118 and the DGTIC project LANCAD-UNAM-DGTIC-104. LC was sponsored by the Mexican postdoctoral fellowship program of the CONACYT-SENER fund for energetic sustainability. D. dCN was sponsored by the Office of Fusion Energy Sciences of the U.S. Department of Energy at Oak Ridge National Laboratory, managed by UT- Battelle, LLC, for the U.S. Department of Energy under Contract No. DE-AC05–00OR22725. We thank the Referees for their thorough review of this MS.

### Appendix A: KORC's Guiding-Center Solver

We follow guiding-center (GC) RE in KORC using the the relativistic Hamiltonian GC model of Ref. 27, which was used in Ref. 12, too. The GC equations of motion for a particle of charge $q$ and mass $m$ are given by:

$$\frac{d\boldsymbol{x}}{dt} = \frac{p_\parallel}{m\gamma_{GC}}\frac{\boldsymbol{B}^*}{B^*_\parallel} + \boldsymbol{E}^* \times \frac{\boldsymbol{b}}{B^*_\parallel} , \tag{A1}$$

$$\frac{dp_\parallel}{dt} = q\boldsymbol{E}^* \cdot \frac{\boldsymbol{B}^*}{B^*_\parallel} , \tag{A2}$$

where $p_\parallel = \gamma_{GC} m\boldsymbol{v} \cdot \boldsymbol{b}$ is the parallel component of the particle's momentum, $\boldsymbol{v}$ is the particle's velocity, $\boldsymbol{b}$ is the unitary vector along the magnetic field at the particle's position, $\gamma_{GC} = \sqrt{1 + 2\mu B/mc^2 + p_\parallel^2/(mc)^2}$ is the GC relativistic factor, $\mu = \gamma_{GC}^2 m v_\perp^2/2B$ is the magnetic moment of the particle, $v_\perp$ is the perpendicular component of the particles velocity, and $B$ is the intensity of the magnetic field at the particle's position. Eqs. (A1) and (A2) use the effective electric and magnetic fields given by:

$$\boldsymbol{B}^* = \boldsymbol{B} + \frac{p_\parallel}{q}\nabla \times \boldsymbol{b} , \tag{A3}$$

$$\boldsymbol{E}^* = \boldsymbol{E} - \frac{1}{q}\left[mc^2\nabla\gamma_{GC} - p_\parallel\frac{d\boldsymbol{b}}{dt}\right] . \tag{A4}$$

In our simulations, $\boldsymbol{B}$ refers either to the equilibrium magnetic field $\boldsymbol{B}(r,\theta)$ or to the perturbed magnetic field $\boldsymbol{B}(r,\theta) + \delta\boldsymbol{B}(r,\theta,\zeta)$.

In KORC, we solve the set of Eqs. (A1)–(A4) using the adaptive stepsize Runge–Kutta, Dormand–Prince

method[28]. In RE simulations where the energy and toroidal momentum is conserved (non-perturbed magnetic field case), we track these quantities and chose the initial time step that will give good conservation properties. Using the Lagrangian of Eq. (6.19) of Ref. 27 and the equilibrium magnetic field of Eq. (1) we obtain the GC toroidal moment of the particles:

$$p_\zeta = -\frac{q\kappa\varepsilon^2 B_0}{2q_0}\log\left(1+\frac{r^2}{\varepsilon^2}\right) + p_\parallel\left(R_0 + r\cos(\vartheta)\right)b_\zeta \ , \tag{A5}$$

where $b_\zeta$ is the toroidal component of the unitary vector along the magnetic field at the particle's position. The energy of the GC particles is defined as $\mathcal{E} = \gamma_{GC}mc^2$. In Fig. 14 we show the conservation of energy defined as $\Delta\mathcal{E} = 100\times\langle(\mathcal{E}(t=0)-\mathcal{E}(t))/\mathcal{E}(t=0)\rangle$, with $\mathcal{E}(t=0)$ the initial energy of the RE. The average $\langle\cdot\rangle$ in $\Delta\mathcal{E}$ is the ensemble average over all confined RE in the simulation. Similarly, we show the conservation of $p_\zeta$ defined as $\Delta p_\zeta = 100\times\langle(p_\zeta(t=0)-p_\zeta(t))/p_\zeta(t=0)\rangle$. The simulation in this figure is a 1 ms simulation of 1 MeV RE with five initial pitch-angles $\vartheta_0 = 5°, 10°, 20°, 30°$, and $40°$. The number of simulated particles is $N_{sim} = 10,000$, and the initial spatial condition of the GC RE is uniform in a torus of radius $r = a$, centered at $R_0$, see Sec. II for details. The initial time step is set to $\Delta t = \tau_{RE}$, where $\tau_{RE} = 2\pi/\Omega_{RE}$ is the relativistic gyro-period, $\Omega_{RE} = eB_0/\gamma m_e$. As it can be seen from Fig. 14, $\Delta\mathcal{E} \sim \pm 10^{-8}$ %, while $\Delta p_\zeta \sim \pm 10^{-7}$ % This good conservation of the magnetic moment prevent spurious radial transport of RE that occurs when $p_\zeta$ is not well conserved. In all the GC simulations reported in this manuscript, we have chosen the initial time step so that we obtain similar conservation properties.

In Fig.15 we show a one-to-one comparison between FO and GC orbits of RE with initial energy $\mathcal{E}_0 = 1$ MeV, 10 MeV, and 25 MeV moving in the equilibrium magnetic field of Eq. (1). Blue (red) lines show FO (GC) orbits. The initial pitch-angle of these RE is set to $\vartheta_0 = 40°$. The magnetic moment $\mu$ of the GC particles is calculated using the magnetic field at the initial particle's position. The initial gyro-phase of the FO particles is random. Initially, the GC relativistic factor is set to the value of the actual, FO relativistic factor, $\gamma_{GC} = \gamma$. As it can be seen, the agreement between FO and GC orbits is quite good, with small differences due to the initial random gyro-phase of the FO particles.

[1]T. Hender, J. Wesley, J. Bialek, A. Bondeson, A. Boozer, R. Buttery, A. Garofalo, T. Goodman, R. Granetz, Y. Gribov, O. Gruber, M. Gryaznevich, G. Giruzzi, S. Günter, N. Hayashi, P. Helander, C. Hegna, D. Howell, D. Humphreys, G. Huysmans, A. Hyatt, A. Isayama, S. Jardin, Y. Kawano, A. Kellman, C. Kessel, H. Koslowski, R. L. Haye, E. Lazzaro, Y. Liu, V. Lukash, J. Manickam, S. Medvedev, V. Mertens, S. V. Mirnov, Y. Nakamura, G. Navratil, M. Okabayashi, T. Ozeki, R. Paccagnella, G. Pautasso, F. Porcelli, V. Pustovitov, V. Riccardo, M. Sato, O. Sauter, M. Schaffer, M. Shimada, P. Sonato, E. Strait, M. Sugihara, M. Takechi, A. Turnbull, E. Westerhof,

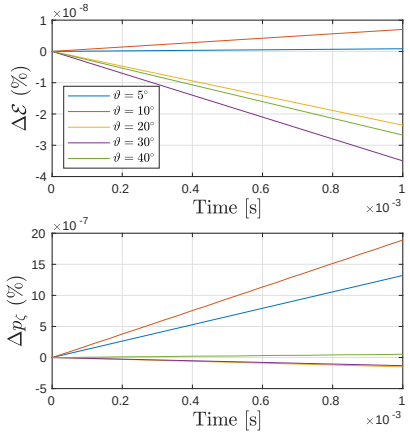


FIG. 14. Energy and toroidal momentum conservation of KORC's GC solver in a 1 ms simulation of 1 MeV RE with five initial pitch-angles $\vartheta_0 = 5°, 10°, 20°, 30°$, and $40°$. The number of simulated particles is $N_{sim} = 10,000$, and the initial spatial condition of the GC RE is uniform in a torus of radius $r = a$, centered at $R_0$. The initial time step is set to $\Delta t = \tau_{RE}$.

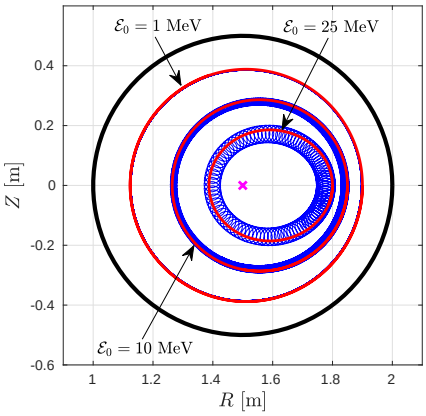


FIG. 15. One-to-one comparison between FO and GC orbits of RE with $\mathcal{E}_0 = 1$ MeV, 10 MeV, and 25 MeV moving in the equilibrium magnetic field of Eq. (1). Blue (red) lines show FO (GC) orbits. The initial pitch-angle of all particles is $\vartheta_0 = 40°$. The thick black line shows the LCFS, and the magenta cross the position of the magnetic axis.

D. Whyte, R. Yoshino, H. Zohm, , D., and ITPA MHD, Disruption and Magnetic Control Topical Group, Nucl. Fusion **47**, S128 (2007).
[2]M. Lehnen, A. Alonso, G. Arnoux, N. Baumgarten, S. Bozhenkov, S. Brezinsek, M. Brix, T. Eich, S. Gerasimov, A. Huber, S. Jachmich, U. Kruezi, P. Morgan, V. V. Plyusnin, C. Reux, V. Riccardo, G. Sergienko, and M. Stamp, Nucl. Fusion **51**, 123010 (2011).
[3]E. Hollmann, M. Austin, J. a. Boedo, N. Brooks, N. Commaux, N. Eidietis, D. a. Humphreys, V. a. Izzo, a. N. James, T. Jernigan, a. Loarte, J. Martin-Solis, R. a. Moyer, J. Muñoz-Burgos, P. Parks, D. Rudakov, E. Strait, C. Tsui, M. a. Van Zeeland, J. Wesley, and J. Yu, Nucl. Fusion **53**, 083004 (2013).
[4]N. Commaux, L. Baylor, T. Jernigan, E. Hollmann, P. Parks, D. Humphreys, J. Wesley, and J. Yu, Nucl. Fusion **50**, 112001 (2010).
[5]N. Commaux, L. Baylor, S. Combs, N. Eidietis, T. Evans, C. Foust, E. Hollmann, D. Humphreys, V. Izzo, A. James, T. Jernigan, S. Meitner, P. Parks, J. Wesley, and J. Yu, Nucl. Fusion **51**, 103001 (2011).
[6]A. Lvovskiy, C. Paz-Soldan, N. Eidietis, A. Molin, X. Du, L. Giacomelli, J. Herfindal, E. Hollmann, L. Martinelli, R. Moyer, M. Nocente, D. Rigamonti, D. Shiraki, M. Tardocchi, and K. Thome, Plasma Phys. Control. Fusion **60**, 124003 (2018).
[7]A. Lvovskiy, W. Heidbrink, C. Paz-Soldan, D. Spong, A. D. Molin, N. Eidietis, M. Nocente, D. Shiraki, and K. Thome, Nucl. Fusion **59**, 124004 (2019).
[8]W. Heidbrink, C. Paz-Soldan, D. Spong, X. Du, K. Thome, M. Austin, A. Lvovskiy, R. Moyer, R. Pinsker, and M. Zeeland, Plasma Phys. Control. Fusion **61**, 014007 (2019).
[9]C. Paz-Soldan, N. Eidietis, E. Hollmann, P. Aleynikov, L. Carbajal, W. Heidbrink, M. Hoppe, C. Liu, A. Lvovskiy, D. Shiraki, D. Spong, D. Brennan, C. Cooper, D. del-Castillo-Negrete, X. Du, O. Embreus, T. Fulop, J. Herfindal, R. Moyer, P. Parks, and K. E. Thome, Nucl. Fusion **59**, 066025 (2019).
[10]R. B. White and Y. Wu, "Collisionless transport in a stochastic magnetic field," Plasma Physics and Controlled Fusion **35**, 595–599 (1993).
[11]V. A. Izzo, E. M. Hollmann, A. N. James, J. H. Yu, D. A. Humphreys, L. L. Lao, P. B. Parks, P. E. Sieck, J. C. Wesley, R. S. Granetz, G. M. Olynyk, and D. G. Whyte, Nucl. Fusion **51**, 063032 (2011).
[12]C. Sommariva, E. Nardon, P. Beyer, M. Hoelzl, G. Huijsmans, and D. V. Vugt, Nucl. Fusion **58**, 016043 (2018).
[13]L. Carbajal and D. del-Castillo-Negrete, Plasma Phys. Control. Fusion **59**, 124001 (2017).
[14]D. del-Castillo-Negrete, L. Carbajal, D. Spong, and V. Izzo, Phys. Plasmas **25**, 056104 (2018).
[15]L. Carbajal, D. del-Castillo-Negrete, D. Spong, S. Seal, and L. Baylor, Phys. Plasmas **24**, 042512 (2017).
[16]A. Wingen, S. Abdullaev, K. Finken, M. Jakubowski, and K. Spatschek, Nucl. Fusion **46**, 941 (2006).
[17]G. Papp, M. Drevlak, T. Fülöp, and P. Helander, Nucl. Fusion **51**, 043004 (2011).
[18]V. Izzo and P. Parks, Phys. Plasmas **24**, 060705 (2017).
[19]H. Mynick and J. Strachan, Phys. Fluids **24**, 695 (1981).
[20]T. Hauff and F. Jenko, "Runaway electron transport via tokamak microturbulence," Physics of Plasmas **16** (2009), 10.1063/1.3243494.
[21]S. Konsta, E. Hirvijoki, J. Decker, J. Varje, and T. Kurki-Suonio, "An advection-diffusion model for cross-field runaway electron transport in perturbed magnetic fields," Plasma Physics and Controlled Fusion **58** (2016), 10.1088/0741-3335/58/12/12501
[22]H. Mynick, Phys. Fluids B **5**, 1471 (1993).
[23]D. del-Castillo-Negrete and L. Chacón, Physics of Plasmas **19**, 056112 (2012).
[24]A. Lichtenberg and M. Lieberman, *Regular and Stochastic Motion*, Applied Mathematical Sciences (Springer New York, 1989).
[25]I. Entrop, R. Jaspers, N. J. Lopez-Cardozo, and K. H. Finken, Plasma Phys. Control. Fusion **41**, 377 (1999).
[26]A. Y. Aydermir, Phys. Plasmas **1**, 882 (1994).
[27]R. J. Cary and A. J. Brizard, "Hamiltonian theory of guiding-center motion," Reviews of Modern Physics **81**, 693–738 (2009).
[28]W. H. Press, S. A. Teukolsky, B. P. Flannery, and W. T. Vetterling, *Numerical Recipes in FORTRAN 77: Volume 1, Volume 1 of Fortran Numerical Recipes: The Art of Scientific Computing* (Cambridge University Press, 1992).

PLEASE CITE THIS ARTICLE AS DOI: 10.1063/1.5135588

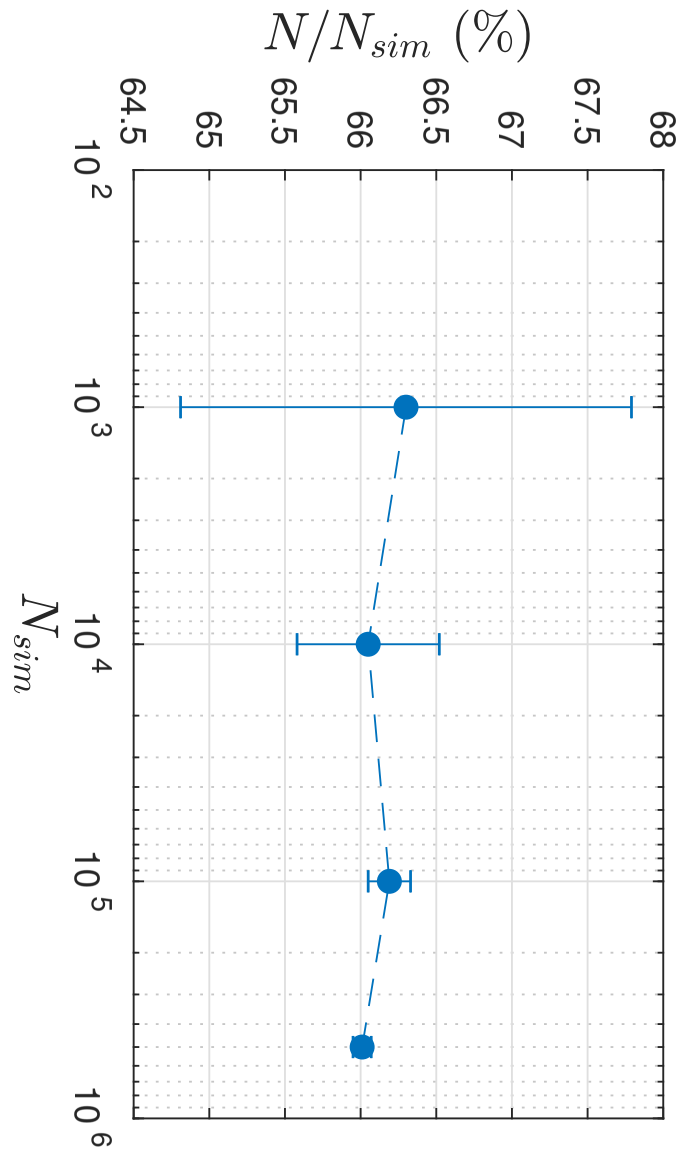

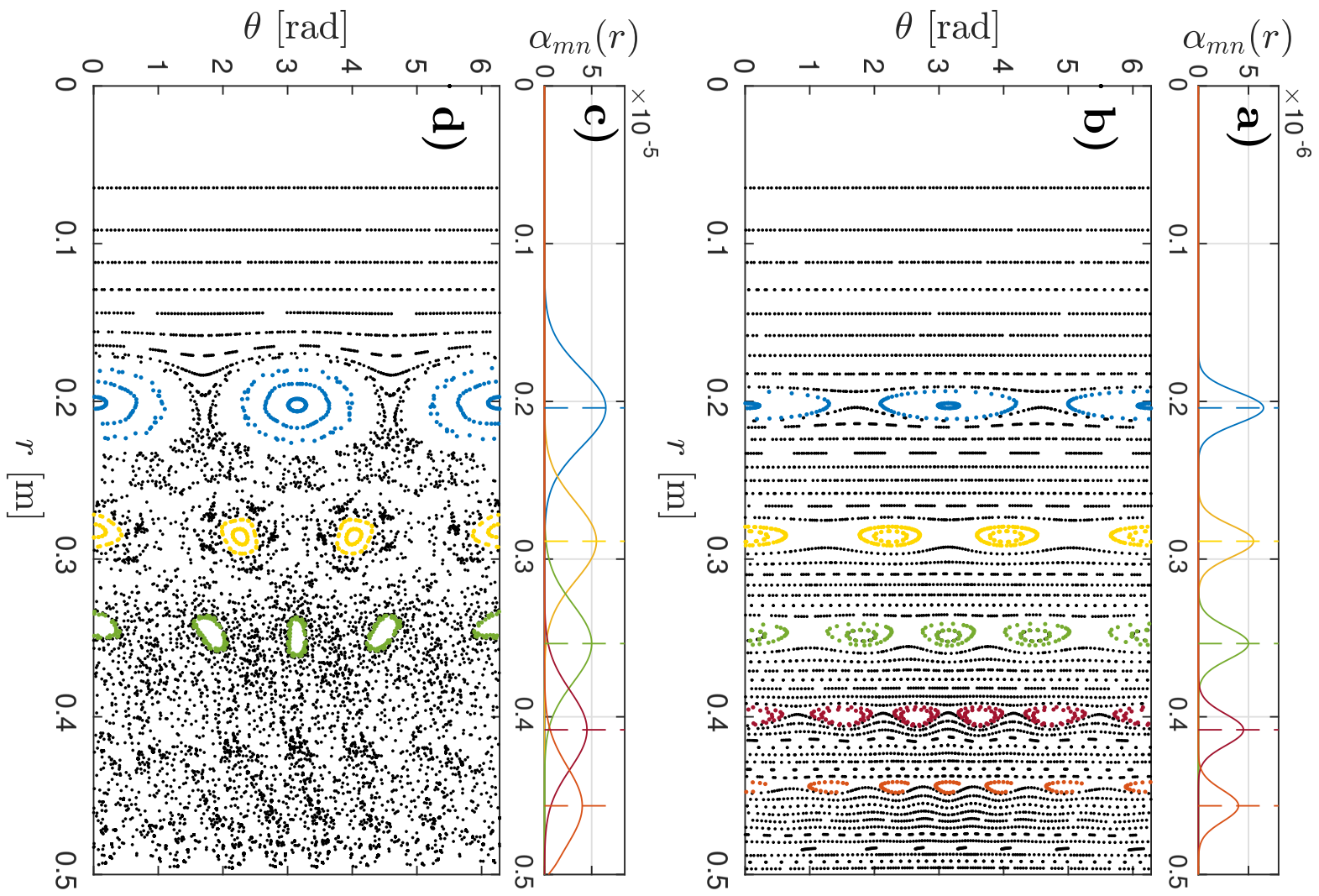

PLEASE CITE THIS ARTICLE AS DOI: 10.1063/1.5135588

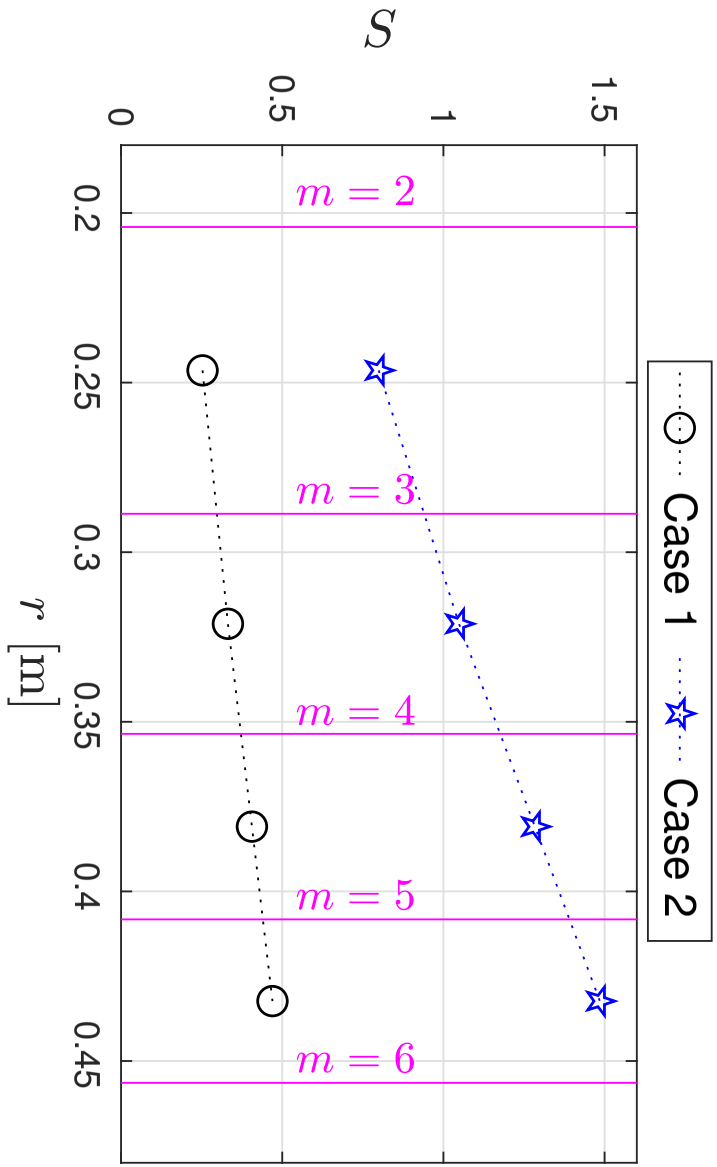

PLEASE CITE THIS ARTICLE AS DOI: 10.1063/1.5135588

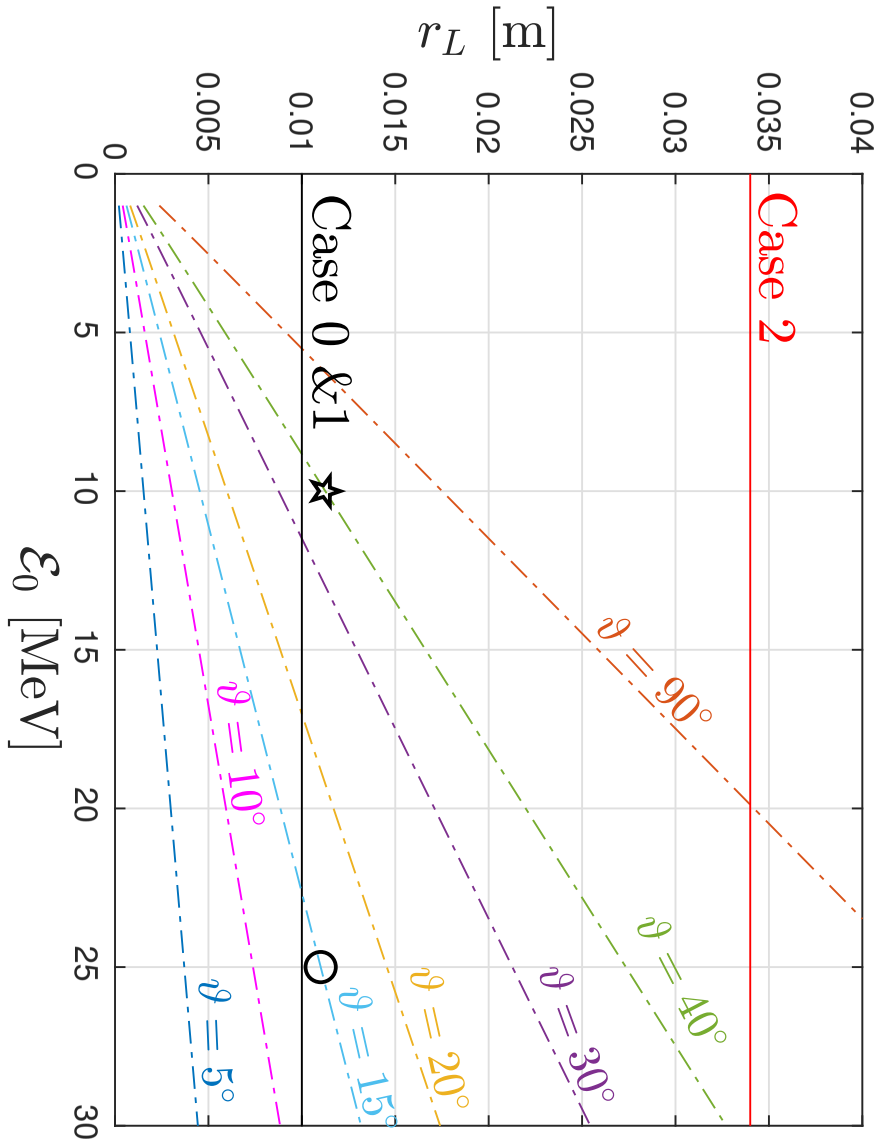

PLEASE CITE THIS ARTICLE AS DOI: 10.1063/1.5135588